ARTICLE OPEN

Check for updates

A machine learning microstructurally predictive framework for the failure of hydrided zirconium alloys

Tamir Hasan[1]✉, Laurent Capolungo[2]✉ and Mohammed Zikry[1]✉

Hydride precipitation within zirconium alloys affects ductility and fracture behavior. The complex distribution of hydrides and their interaction with defects, such as dislocations, have a significant role in crack nucleation and failure. Hence, there is substantial variability in the microstructural behavior of hydrided zirconium. A deterministic fracture model coupled to a dislocation-density based crystalline plasticity approach was used to predict failure. Deterministic simulations were used to develop a database of crack initiation for representative microstructural characteristics, such as texture, crystalline structure, hydride orientations and spacing, and hydride geometry. The machine learning (ML) analysis is based on Extreme Value Theory (EVT) and a Bayesian based Gaussian Process Regression (GPR). Fracture probability is significantly influenced by hydride orientation and dislocation-density interactions. Furthermore, surrogate reduced order models (ROM) models were used to predict the likelihood of failure. This approach provides a ML framework to predict failure at different physical scales.

npj Materials Degradation (2023)7:22 ; https://doi.org/10.1038/s41529-023-00344-7

INTRODUCTION

Zirconium alloys play a significant role as cladding and protective layers for high temperature applications, such as nuclear reactors, hypersonics, and marine systems[1,2]. These alloys are generally corrosion resistant at high temperatures, possess favorable high-temperature mechanical characteristics, and are resistant to thermal neutrons and irradiation. Zirconium alloys can, however, thermo-mechanically degrade through the formation of hydrides due to high temperature water exposure and long-term storage[2–5] and during loss-of-coolant accidents (LOCA)[6] for nuclear applications. Furthermore, these hydrides have different crystalline structures than the parent zirconium alloy[5], which renders these material systems as multiphase and heterogenous.

Critically, hydride orientation, morphology, distribution, texture, crystalline structures, spacing, and dislocation-densities all have interrelated effects on thermo-mechanical behavior at scales ranging from the nano to the micro[7–9], and collectively affect fracture nucleation and propagation[5,7,8]. Hsu et al.[9] investigated fracture toughness on thin-walled tubing for different temperatures. They determined that hydride orientation, hydrogen content, and temperature were all factors influencing fracture toughness in hydrided zirconium alloys and concluded that the presence of radial hydrides reduces the fracture toughness at room temperature when compared with distributions of circumferential hydrides, with J_{max} values of pure circumferentially hydrided samples up to 40 kJ/m^2, and values for samples with 52.2% radial hydrides as low as 11 kJ/m^2[9]. Kim et al. performed ring compression tests (RCTs) on both circumferentially and radially hydrided zirconium alloys. Their results indicate that radially oriented hydrides are more likely to fracture than circumferentially oriented hydrides because of the favorable crack propagation pathways associated with radial hydride arrangements[10]. Experiments by Pierron et al.[11] show that the elongated grains associated with cold worked and stress relieved (CWSR) samples compared with a recrystallized process had little impact on fracture toughness. They also observed void nucleation ahead of a crack in a hydrided material, which indicates that voids can be sites of multiple ductile crack nucleation regions, and this eventually can lead to crack propagation and material rupture[11]. Hydride lengths and hydride spacing have also been shown to affect fracture strengths. For lengths of less than 25 μm, ultimate tensile stresses in the in Zr-2.5 Nb alloys can decrease by approximately 1.4 MPa for every 1 μm increase in average hydride length[12].

Other approaches for understanding the relationship between hydride behavior and fracture have focused on Delayed Hydride Cracking (DHC)[13,14]. DHC occurs when hydrogen slowly diffuses to a preexisting crack tip region, thereby resulting in crack propagation. Hydride formation at preexisting crack tips leads to further fracture growth after a delay due to the steadily increasing presence of the formed hydrides at the crack tip. Sharma et al.[15] investigated the fracture behavior of hydrided zirconium alloy tubing material using mechanical testing. They were able to change the hydride morphology by annealing a system with 100% radial hydrides. Varying the annealing temperature between 300 °C, 325 °C, and 350 °C influenced the percentage of circumferential hydrides. Their findings indicate that a 100% circumferentially hydrided material has more than four times higher critical crack lengths when compared with a 100% radially hydrided material, at room temperature. At higher temperatures (250 °C and above), the radially hydrided critical crack length increases to match that of the circumferential material. This indicates that the greatest variation between the fracture response of circumferential and radial hydrided materials occurs at room temperature. Additionally, the fracture toughness of predominantly radially hydrided material was approximately three times lower than that of the circumferentially hydrided material at room temperature.[15]. These experiments clearly indicate that microstructural characteristics, such as texture and dislocation-densities, need to be quantified to understand how they specifically affect fracture nucleation and evolution. Furthermore, most of these experimental investigations pertain to crack propagation in systems with preexisting cracks as opposed to crack nucleation in hydrided systems, since crack nucleation is difficult, if not impossible, to

[1]North Carolina State University, Raleigh, NC, USA. [2]Los Alamos National Laboratory, New Mexico, NM, USA. ✉email: tamir.hasan@gmail.com; laurent@lanl.gov; zikry@ncsu.edu

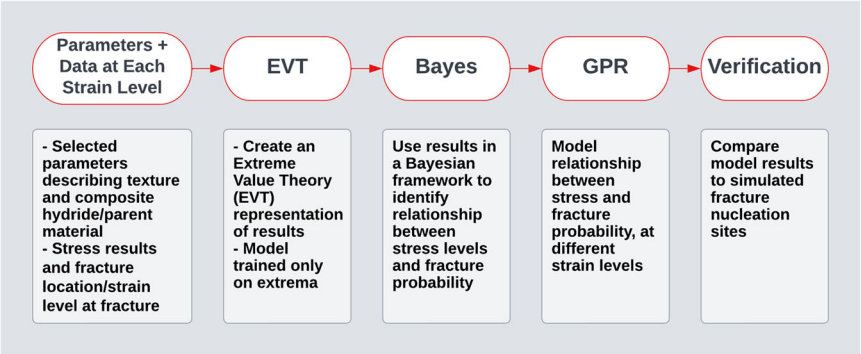

Fig. 1 An outline of the ML fracture failure probability model.

experimentally quantify. Thus, modeling efforts can provide further insights into fundamental fracture mechanisms.

In[16], finite element (FE) models were used to understand how hydrogen embrittlement affects cracking and DHC for pre-cracked materials. Hydride-induced fracture depends on the hydride microstructure that formed during operation, hydrogen diffusion to the crack tip is also observed for fractured specimens and this can also affect crack propagation.

Jernkvist[17] also investigated DHC for pre-cracked or notched zirconium and titanium alloys for different hydride orientations and volume fractions. Suman[18] investigated the impact of crack and hydride lengths on crack propagation in simulated DHC. While these studies have provided valuable insights, the link between dislocation activity and fracture nucleation have not yet been understood. Other insights were provided from Olsson et al.[19], where fracture toughness was modeled with an ab initio-based approach using density functional theory (DFT). Their findings indicated that increasing hydrogen content reduced ductility by inhibiting dislocation nucleation and accumulation. This provides a foundation on which to base larger scale fracture simulations. While these approaches all provide valuable insights, a comprehensive deterministic modeling approach that incorporates microstructural variation, the impact of dislocation-densities on fracture at the microstructural scale is needed to provide insights and understanding of fracture nucleation that account for intergranular and transgranular failure. Furthermore, the question of how to obtain statistical information pertaining to deterministic fracture models has not yet been clearly addressed.

As these various experimental and computational investigations indicate, the thermo-mechanical fracture behavior of hydrided zirconium alloys is dominated by microstructural mechanisms, such as hydride orientation, material orientation, grain morphology, texture, hydride volume fraction and defects, such as dislocation densities, which collectively can affect multiple crack nucleation and failure. Deterministic models have provided insightful understanding of how fracture at the microstructural scale leads to failure [cf. 19,20], but they have not yet yielded a comprehensive and quantitative description of microstructure-induced epistemic uncertainty.

Different machine learning (ML) methods have also been used to model material characteristics derived from deterministic models and experiments. ML provides a data driven approach, through supervised and unsupervised approaches, to determine dominant properties or behavior from experimentally or computationally obtained measurements and predictions. For example, regression neural networks and reduced ordered models (ROMs) have been used to represent inelastic deformation in crystals and defect models, such as dislocations and cracks, can be used to guide predictions of material response for different loading conditions[20]. One advantage of creating ROMs for material models is the ability to use the resulting insights with limited computational cost for larger scale simulations. For example, models predicting failure should account for local variabilities among material properties and behavior, in addition to geometrical effects. Hunter used multilayer perceptrons (MLP; artificial neural networks) on a dataset based on FE element simulations of a simple homogenous and elastic block-like material with pre-existing cracks to determine how fracture can occur[21]. Crystal plasticity simulations and fracture modeling are often based on undetermined and unknown parameters that cannot be obtained experimentally or computationally. Examples for crystal plasticity can include determining how dislocation-densities accumulate at GBS and interfaces of hydrides, precipitates, and grain-boundaries[22,23]. Numerous ML techniques have been used in mechanics, materials science, and applied mathematics. Commonly used methods are k-nearest neighbors (k-NN), decision trees (DT), random forest (RF), artificial neural networks (ANN), Bayesian networks, Gaussian Process Regression, and deep learning[24–26].

Other approaches have attempted a more direct path of using deep learning methods to predict stress and other material properties when given a purely spatial input of stresses, strains, elastic strains, and plastic strains. These methods have shown promise in simplifying models related to the elastic solution of beam and plates[27,28]. These methods alone, however, have not been used to obtain statistically significant predictions for complex material systems that span multiple physical scales, such as hydrided systems.

There is, therefore, a need for measurable ML link to microstructural mechanisms and characteristics, such that dominant microstructural mechanisms can be identified. Hence, we will introduce a ROM to predict failure probability as a function of the material characteristics. The ROM is obtained by mining a database of crack responses of representative volume elements. Specifically, the database is constructed using FEM simulations based on our previously detailed and validated microstructural deterministic fracture approaches that couple crystalline plasticity and a microstructurally based fracture nucleation framework. We will use a multiparametric ROM approach to generalize the results and *explicitly* determine the probability of material failure.

Figure 1 shows the proposed approach to develop the fracture probability models. The starting points are the deterministic outputs from the dislocation-density based crystalline plasticity simulations. The exploration and understanding of many dimensions of the parametric space, such as dislocation density accumulation, texture, shear-slip strains, and hydride distributions, structure, and orientation, that are difficult, if not impossible, to obtain experimentally, will provide the data necessary for this approach. Table 2 shows the parameters modified in these simulations and their range of values. The method then consists of expressing the results in a compact form using Extreme Value Theory (EVT), a Bayesian approach for developing the fracture

criteria for probability, and a modeling scheme based on Gaussian Process Regression (GPR) to obtain failure probabilities and the uncertainty associated with the predictions. The models were then verified on data that was not used to train them using a test-train split method. The overall objective of this study is to provide a database of deterministic FE fracture approaches that explore a wide parameter space representing variations within hydrided zirconium material systems, and then to develop Bayesian models, based on these physically based datasets, to identify the dominant microstructural characteristics and mechanisms that result in the failure at different physical scales.

This paper is organized as follows: the multiple slip dislocation-density crystalline plasticity formulation and derivation of dislocation-density evolution equations and mobile and immobile dislocation-density evolution are presented in Section I; the computational and statistical approaches are outlined in Section II; the results and discussion of the fracture nucleation probabilities for different material configurations are given in Section III.

METHODS

Multiple-slip crystal plasticity dislocation-density

We will only present a brief outline of the dislocation-density crystalline approach used in the present work. A detailed presentation can be found in Zikry and Kao[29] and Shanthraj and Zikry[30]. In this approach, it is assumed that, for a given deformed state of the material, the total dislocation-density of a particular slip system a, ρ^a, can be additively decomposed into a mobile and an immobile dislocation-density, ρ^a_m and ρ^a_{im}. Based on a conservation of mass for mobile and immobile dislocation densities, during an increment of strain on a slip system, a mobile dislocation-density rate is generated, and an immobile dislocation-density rate is annihilated[30]. Furthermore, the mobile and immobile dislocation-density rates can be coupled through the formation and destruction of junctions as the stored immobile dislocations act as obstacles for evolving mobile dislocations.

Evolution equations for mobile and immobile dislocation densities can then be obtained by considering the generation, interaction, immobilization, and annihilation of dislocation densities to obtain evolution equations. These equations are dependent on the plastic deformation rate and inform the evolution of mobile and immobile dislocation densities as

$$\frac{d\rho^a_m}{dt} = |\dot{\gamma}^a|\left(\frac{g^a_{sour}}{b^2}\left(\frac{\rho^a_{im}}{\rho^a_m}\right) - g^a_{mnter-} - \rho^a_m - \frac{g^a_{immob-}}{b}\sqrt{\rho^a_{im}}\right), \quad (1)$$

$$\frac{d\rho^a_{im}}{dt} = |\dot{\gamma}^a|\left(g^a_{mnter+}\rho^a_m + \frac{g^a_{immob+}}{b}\sqrt{\rho^a_{im}} - g_{recov}\rho^a_{im}\right), \quad (2)$$

where g_{sour} is the coefficient pertaining to an increase in the mobile dislocation density due to dislocation sources, g_{mnter} is the coefficient related to the trapping of mobile dislocations due to forest intersections, cross slip around obstacles, or dislocation interactions, g_{recov} is a coefficient related to the rearrangement and annihilation of immobile dislocations, and g_{immob} is related to the immobilization of mobile dislocations. These coefficients, which have been nondimensionalized, are summarized in Table 1, where f_0, and φ are geometric parameters. H_0 is the reference activation enthalpy, l_c is the mean free path of a gliding dislocation, b is the magnitude of the Burgers vector, and ρ_s is the saturation density. It should be noted that these coefficients are functions of the immobile and mobile densities, and hence are updated as a function of the deformation mode.

Orientation relationships (ORs)

ORs are needed for the multiphase system, such that the fcc hydrides can be represented within the hcp matrix for accurate interphase behavior. The approach for incorporating ORs between the zirconium hydrides and hcp parent material was detailed by Mohamed and Zikry[31]. In ref. [31], it was shown that there can be 36 unique ORs between fcc and hcp material systems. Here, we use the most commonly experimentally relationship[32] as

$$(0001)_{hcp}//(111)_{fcc}\ and\ \left[11\bar{2}1\right]_{hcp}//\left(\bar{1}10\right)_{fcc}. \quad (3)$$

Table 1. Coefficients for dislocation-density equations (Eqs. 1, 2).

Coefficients	Expression
g^a_{sour}	$b^a\varphi\sum_\beta\sqrt{\rho^\beta_{im}}$
g^a_{mnter-}	$l_c f_0\sum_\beta\sqrt{a_{\alpha\beta}}\left[\frac{\rho^\beta_m}{\rho^a_m b^a}+\frac{\dot{\gamma}^\beta}{\dot{\gamma}^a b^\beta}\right]$
g^a_{immob-}	$\frac{l_c f_0}{\sqrt{\rho^a_{im}}}\sum_\beta\sqrt{a_{\alpha\beta}}\rho^\beta_{im}$
g^a_{mnter+}	$\frac{l_c f_0}{\dot{\gamma}^a\rho^a_m}\sum_{\beta,\gamma} n^{\beta\gamma}_\alpha\sqrt{a_{\beta\gamma}}\left[\frac{\rho^\gamma_m\dot{\gamma}^\beta}{b^\beta}+\frac{\rho^\beta_m\dot{\gamma}^\gamma}{b^\gamma}\right]$
g^a_{immob+}	$\frac{l_c f_0}{\dot{\gamma}^a\sqrt{\rho^a_{im}}}\sum_\beta n^{\beta\gamma}_\alpha\sqrt{a_{\beta\gamma}}\rho^\gamma_{im}\dot{\gamma}^\beta$
$g^a_{re\ cov}$	$\frac{l_c f_0}{\dot{\gamma}^a}\left(\sum_\beta\sqrt{a_{\alpha\beta}}\frac{\dot{\gamma}^\beta}{b^\beta}\right)e^{\left(\frac{-H_0\left(1-\sqrt{\frac{\rho^a_{im}}{\rho_s}}\right)}{kT}\right)}$

Fracture approach

The fracture method used here is based on crack nucleation within a finite element mesh by splitting the element into two halves along the crack plane using an overlap method. The method to nucleate and propagate cracks was refined by Wu and Zikry[33] for microstructurally based fracture. This method is implemented by monitoring the maximum normal component of traction across all the material cleavage planes. To avoid numerical instability from the instantaneous release of elastic energy within the newly cracked element, a traction-free surface is generated by reducing the nodal forces over a set time step interval until they reach zero. The crack is then nucleated by adding phantom nodes to elements aligned to the crack plane. The detailed approach is given in[33].

Fracture stress nucleation and propagation predictions

The univariate branch of Extreme Value Theory (EVT) is a type of statistics that is focused specifically on large deviations of a parameter from the mean, and hence it is well suited for extreme events, such as fracture nucleation. The applicability of the Gumbel distribution to represent the distribution of maxima is closely related to EVT, since it is exponentially related to maximal events. which indicates that it is likely to be useful if the distribution of the underlying sample data is of the normal or exponential type[20,34].

The generalized extreme value (GEV) distribution[34] is a set of distributions that are designed to capture the distribution of these large deviations. The Gumbel formulation was chosen for this study because it has neither a finite upper bound nor a heavy tail, which is well-suited for fracture nucleation because elemental fracture stresses are conceptually neither expected to accumulate at the extremes without unloading (cracking) nor are large sections of material expected to uniformly aggregate at a particular limit. The Gumbel distribution It is also known as the Type 1 GEV, and

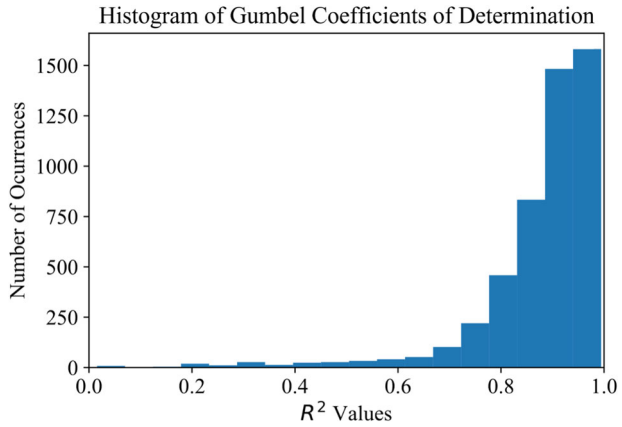

Fig. 2 Pearson Coefficients for the trained Gumbel distributions, $n = 4943$.

the associated probability density function (PDF) is

$$P = \frac{1}{\beta} e^{-(z+e^{-z})}, \; where \, z = \frac{x-\mu}{\beta}. \tag{4}$$

To characterize element-wise stress in the form of a Gumbel distribution, individual element stress responses were recorded at incremental strain levels. The number of values at each stress level were then normalized by element size. The Gumbel r statistical function within the SciPy Python library was then used to fit a Gumbel distribution to the 95th percentile of stress results[34]. To test the adequacy of the fit for the use of Gumbel distributions, the Pearson Coefficients for the individual Gumbel fits were calculated. The Pearson coefficients are a measure between sets of data, and hence it is the ratio between the covariance of variables and the product of their standard deviation; thus, it is essentially a normalized measurement of the covariance[34].

To do this, the probplot function from SciPy[34] was used to generate both an estimate of the quantiles of the sample data and associated quantile predictions of the fitted Gumbel distribution. Filliben's estimate, which is based on calculating the quantiles of the observed data the quantile function for the Gumbel distributions[34,35]. These data were compared and a "goodness of fit" was calculated using the coefficient of determination. A value of 1.0 indicates that the quantiles of both the fitted Gumbel distribution and the observed data match perfectly. 4943 total Gumbel fits were performed; one for every output print interval for each simulation. Figure 2 shows these coefficient of determination values together in histogram format. 90.4% of the values are between 0.75 and 1.0, which indicates that the Gumbel fit is an accurate method to approximate the stress response of the system.

The μ parameters of the Gumbel distributions were individually calculated and used to represent the extrema within the representative volume elements (RVEs) being modeled. The shape parameter also provides valuable information about fat-tailed characteristics, and this information may be used in future studies.

Bayesian framework

Bayes' rule was used to generate a framework for linking stress levels with the associated probabilities of failure. Bayes' Rule is given by Eq. 5:

$$P(A|B) = \frac{P(B|A) \cdot P(A)}{P(B)}. \tag{5}$$

For this study, $P(A)$ and $P(B)$ were the probabilities of a crack forming and of the existence of a stress state at a particular nominal strain level. $P(A)$ was generated by examining the percentage of the database population at a given strain level that had cracked. The probabilities of cracking at various stress states and strain levels were calculated and stored.

Gaussian process regression

Gaussian Process Regression (GPR) was used to represent the Bayesian framework probabilities in a continuous manner. Gaussian ProDifferent GPRs were trained for each strain level to reduce the resulting complexity of the models. The GaussianProcessRegressor function within the SciKit-Learn package was used to train the models[35]. To test the validity of our datasets, the data were split into training and testing segments that comprised 80% and 20%, respectively, of the total data set size. The included scoring function was used to verify the accuracy of the resulting GPRs.

RESULTS AND DISCUSSION

FE models and generated databases

A database of 210 crystal plasticity simulations was generated for this study to identify the variation of stress and fracture characteristics in hydrided zirconium. Each simulation was performed with and without crack nucleation, so that the localized material yielding associated with crack formation would not interfere with the bulk stress measurements performed for this study. The database was populated by randomly modifying five parameters of interest using 4 predefined levels between a minimum value and a maximum value. These parameters are shown in Table 2. These parameters were chosen because they belong to two general categories of interest: (1) material orientation, (2) hydride population geometry and distributions. These categories influence both dislocation-density activity and material fracture[5,12,15,22]. Together, they comprise the material *fingerprint* of individual simulations and are the only differentiating factor between them. The trajectory scheme from the Elementary Effects method implemented using the SAlib library, and was also used as the method of selecting random trajectories throughout the solution space made of all possible material fingerprints[36,37]. These models were designed to emulate the material response of a cladding tube undergoing a uniform internal pressurization. Symmetry boundary conditions were used with plane strain loading. A representative tessellated hydrided volume is shown in Fig. 3. A new multigrain representative volume element (RVE) was developed for each simulation, with a convergent mesh size of approximately 60,000 elements and 49 parent zirconium alloy grains with an average grain diameter of 25 microns. The mesh size was obtained after a detailed mesh convergence analysis. The grain-shapes were generated by Voronoi tessellation[19]. The material properties and hydrided fracture behavior were validated using the work of Mohamed and Zikry[22] and the properties are given in Table 3.

Hydride orientation on crack probability

Crack probabilities at 1.25%, 1.50%, and 1.75% nominal strains were obtained. It should be underscored that these are the global nominal strains, and that the local shear slip associated with different slip systems are significantly higher. For each nominal strain, fracture critical stress levels were varied to understand the impact of fracture critical stress on the resulting crack probabilities. Three categories were used to define hydride orientations: circumferential, radial, and mixed. Circumferential hydrides are parallel to the loading direction, radial hydrides are perpendicular to the loading direction, and mixed hydrides occur in all other orientations.

The fracture stress obtained as a function of the probabilities are shown in Figs. 4–6 for the fracture stress probability

Table 2. Hydride microstructural distributions.

Parameter name	Category of Interest: Fingerprint	Minimum value	Maximum value
Hydride Length	Hydride geometry	0.5E−5 m	3.0E−5 m
Parent Material Orientation	Material Orientation	0°	90°
Hydride Volume Fraction	Hydride geometry	5%	20%
Hydride Orientation	Hydride geometry	0°	90°
Hydride Spacing	Hydride geometry	2.5E−6 m	1.0E−5 m

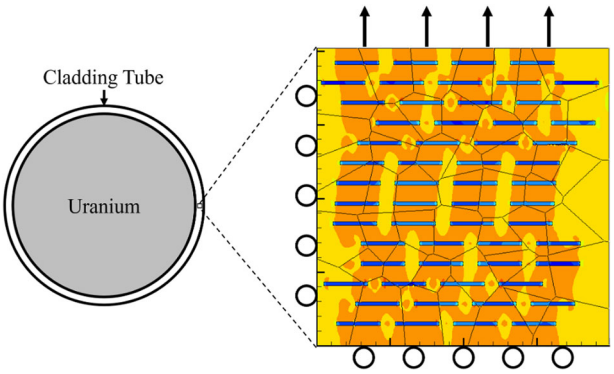

Fig. 3 A cladding tube and loading diagram of a typical multiphase hydrided zirconium alloy representative volume element.

Table 3. Material Properties.

Property	Zircaloy-4	δ-hydrides
Young's modulus (GPa)	35	132
Static yield stress (MPa)	220	220
Poisson's ratio	0.349	
Rate sensitivity coefficient (rate of change of slip rate with respect to each resolved shear stress based on a power law[22])	45	
Initial immobile dislocation density (m^{-2})	1×10^{10}	
Initial mobile dislocation density (m^{-2})	1×10^{7}	
Burger's vector	1×10^{-10}	
Fracture stress (MPa) (N/mm^2)	700	1000
Applied tensile nominal strain (%)	12	800

corresponds to a nucleated crack. The circumferentially hydrided zirconium has reduced fracture probability when compared to radial and mixed hydrided materials at the same stress levels. At the higher strain levels, such as at 1.75% nominal strain, the difference between the fracture probabilities is lower because the impact of aggregate nominal strain on the material as a factor influencing fracture outweighs the impact of hydride orientation. The probability of radial cracks nucleating at lower strains than circumferential hydrides is consistent with experimental observations (cf.[9,10].). These probabilities indicate that hydrided zirconium alloys will eventually nucleate cracks and rupture no matter what the hydride distribution, and this further underscore how hydrided zirconium alloys are always a precursor to failure.

Models describing crack probability as a function of strain and fracture stress

Gaussian Process Regressors (GPRs) were used to generate a uniform function approximation of the relationship between the probability of failure and the fracture stress at various strain levels.

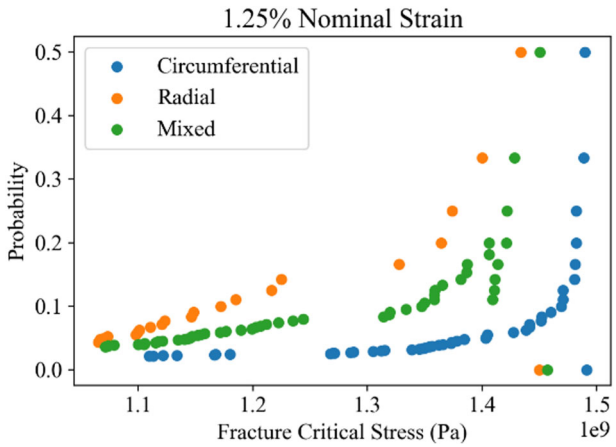

Fig. 4 Bayesian crack probability analysis for 1.25% nominal strain.

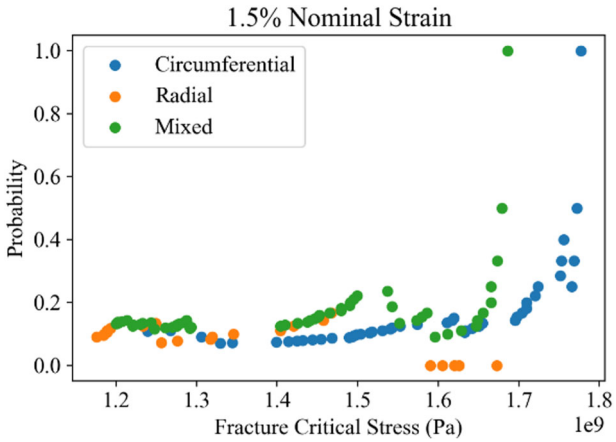

Fig. 5 Bayesian crack probability analysis for 1.50% nominal strain.

The regressor predictions, as a function of the training data, are shown in Figs. 7–10. At lower strain levels, such as 1.25%, fracture probability is low until large fracture stress levels develop in the material at approximately 1.5 GPa. Also note that the shaded areas correspond to the uncertainties or standard deviations associated with the GPR predictions. This is compared with the 2.0% strain level, where any fracture stress level above 1.6 GPa is predicted for failure. This indicates that the fracture stress and the nominal strain both play a significant role in material failure; lower strain levels require higher fracture stresses to fracture and at higher strain levels, lower fracture stresses are required. The lower fracture stress for nucleation is due to the increased ductility associated with increased immobile dislocation density activity. In Fig. 8, the fracture probability does not extend to 1.0 because the sparse nature of the dataset resulted in a lack of sufficient fracture data at this strain level.

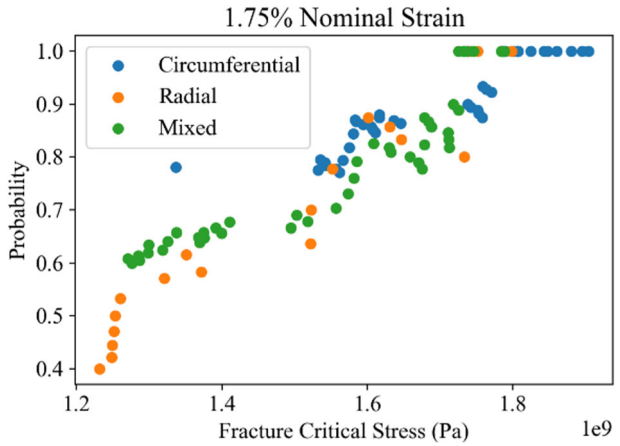

Fig. 6 Bayesian crack probability analysis for 1.75% nominal strain.

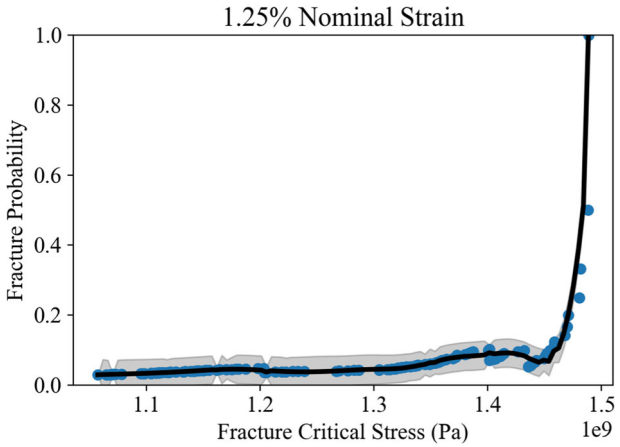

Fig. 7 Fitted GPR representing the failure probability for fracture critical stress levels at 1.25% nominal strain.

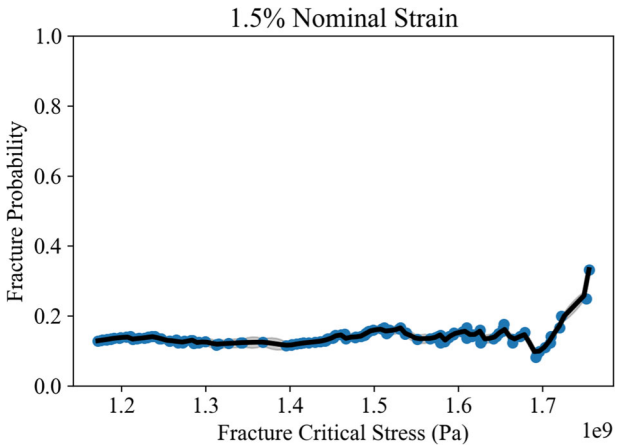

Fig. 8 Fitted GPR representing the failure probability for fracture critical stress levels at 1.5% nominal strain.

Assessing the accuracy distribution of fracture

To test the effectiveness of these ML models, the test-set data were analyzed using the trained GPRs at 1.25%, 1.5%, 1.75% and 2.0% strain, such that the models were tested against data that had not been used to train them, based on the 80-20% training set approach, where we interrogate 20% of the data to assess the

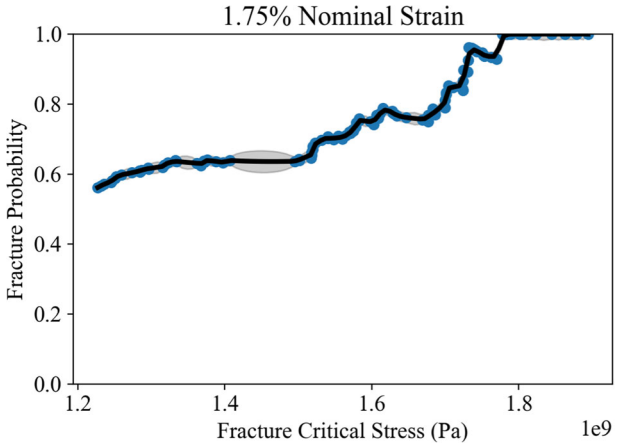

Fig. 9 Fitted GPR representing the failure probability for fracture critical stress levels at 1.75% nominal strain.

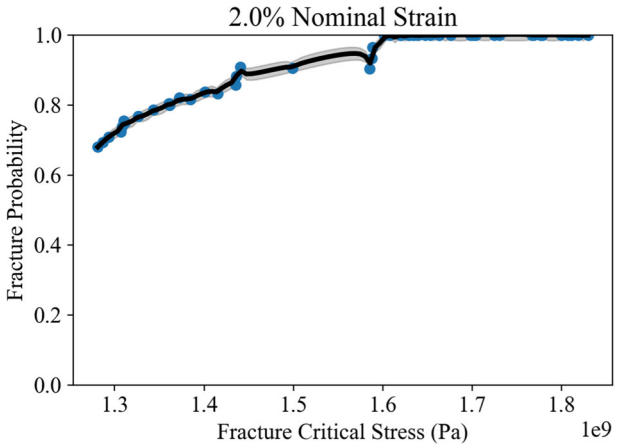

Fig. 10 Fitted GPR representing the failure probability for fracture critical stress levels at 2.0% nominal strain.

probability of failure. Ideally, the models would predict a 100% likelihood of failure at the strain levels that the individual test simulations indicated a failure. The individual probability outputs are shown as the histogram in Fig. 11 to demonstrate the effectiveness of the modeling system on a population of input data. The models demonstrate a high level of accuracy, with all input data indicating a failure probability of least 94%.

Models for crack probability as a function of strain and shear slip

Dislocation-densities play a dominant role in crack nucleation, particularly at the interfaces within multiphase materials, such as hydrided zirconium alloys. Dislocation densities can blunt crack growth directions and nucleation sites[38]. Hence, shear slip, which is the total accumulated slip on all slip systems, was used to determine failure probability in the same manner as fracture critical stress. Figures 12, and 13 show the predictions of failure probability given by the interrogated data. The highest values of shear slip at lower strain levels, such as 1.5%, inhibit crack nucleation, reducing the probability of failure. This is consistent with hydrides, particularly with the fcc crystal structure, being dislocation sources within a material and allowing limited amounts of ductility and crack-blunting until the interface-induced effects become dominant at higher strain levels[22,31,39] (Fig. 14).

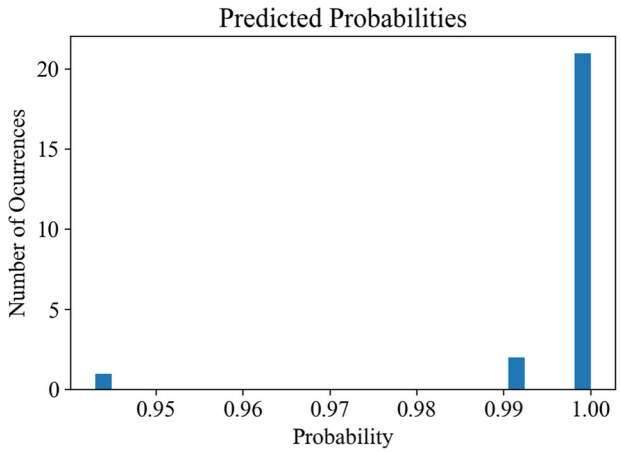

Fig. 11 Predicted probability of failure on test-set data at 1.25%, 1.5%, 1.75% and 2.0% strains. The ideal value is 1.0, or 100% probability.

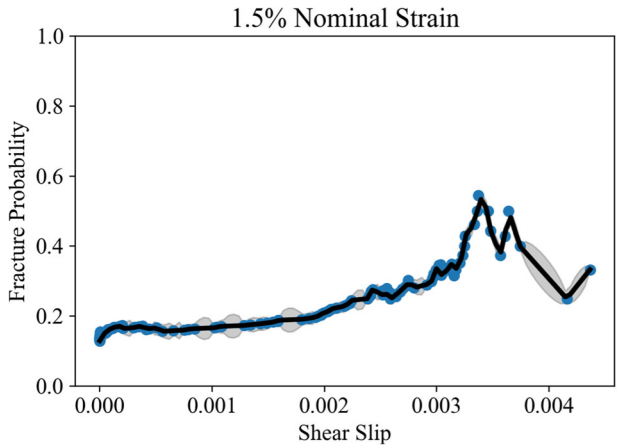

Fig. 12 Fitted GPR representing the failure probability for shear stress levels at 1.5% nominal strain.

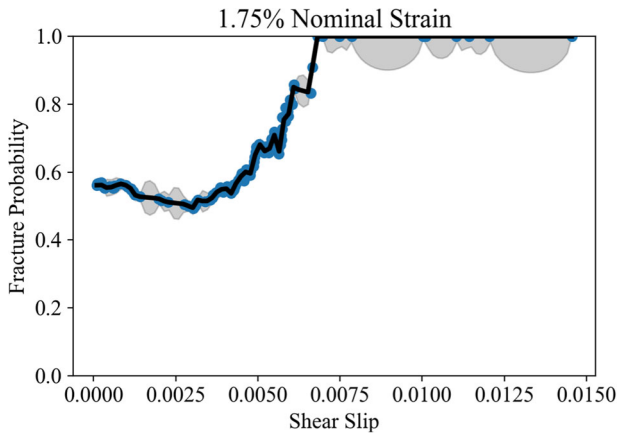

Fig. 13 Fitted GPR representing the failure probability for shear stress levels at 1.75% nominal strain.

Figure 15 shows the failure probability predictions from the models when provided with the already-failed test-set data. While some level of accuracy is observed (all values greater than 68% probability), the predictions are overall less accurate than those trained on fracture critical stresses (99.7% vs. 90.6% average

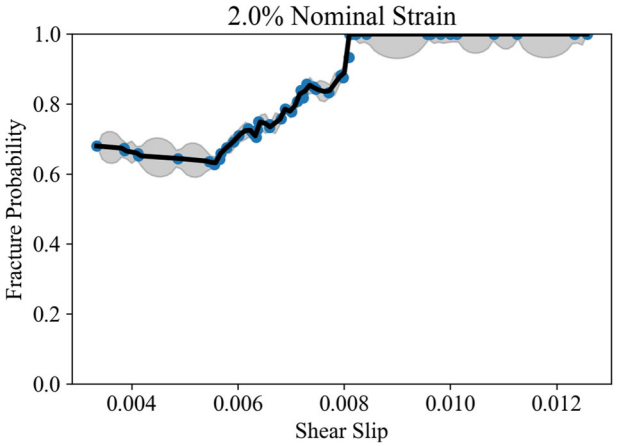

Fig. 14 Fitted GPR representing the failure probability for shear stress levels at 2.0% nominal strain.

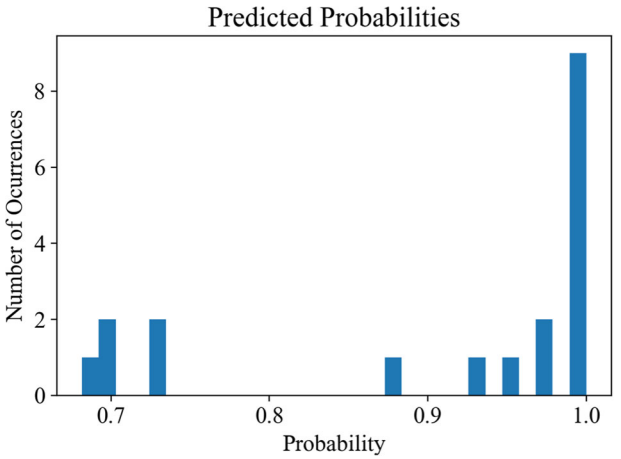

Fig. 15 Predicted probability of failure on test-set data at 1.5%, 1.75% and 2.0% strain levels. The ideal value is 1.0, or 100% probability.

prediction). While this does corroborate that there is a link between dislocation-density activity and fracture probability, it also demonstrates that this link is not as strong as that between fracture critical stress and fracture probability. This is likely because dislocation-density activity that occurs during material strain can alleviate the probability of failure through crack blunting effects but can also be an indicator of the excessive plastic work that leads to fracture, as indicated by Elkhodary and Zikry[40].

Heatmaps predicting probability of failure

These GPRs can be used to generate cracking probability predictions on a spatial element within a mesh where fracture critical stress is known. The knowledge of where cracking is likely to occur is helpful for examining the impact of hydrides in an RVE and for adding additional functionality to simulations where crack nucleation is not modeled. In Fig. 16, the process is visually demonstrated. The normal stress results from the simulation at the strain of interest and is used as element-wise input data to the GPRs. The resulting predictions are then plotted to the same elements, providing a spatial method for interpreting the results. In this case, hydrided regions of the mesh are most likely to crack due to factors such as hydride orientation and spacing. This is

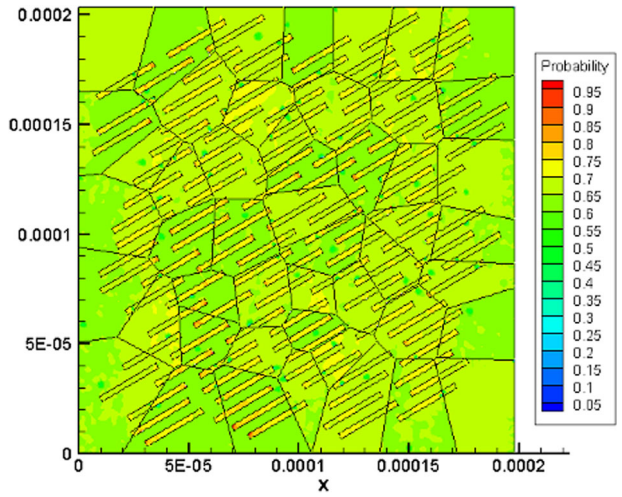

Fig. 16 A sample microstructure showing visual cracking probabilities as a heat map generated by the trained models, showing how cracks are most likely to initiate near hydride tips.

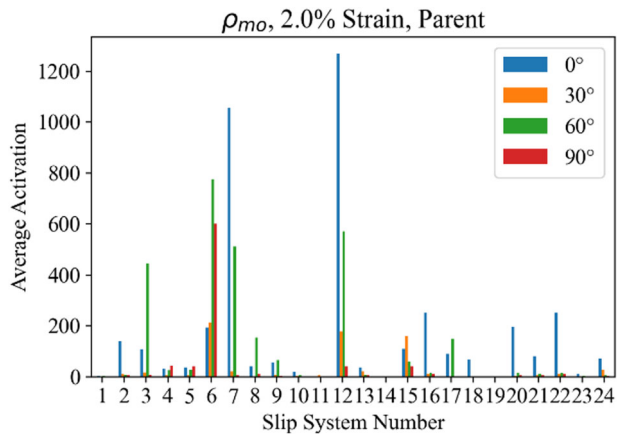

Fig. 17 Average mobile slip system activation for parent material (hcp) at 1.25% nominal strain.

consistent with experimental observations and measurements and fracture predictions[5,12,15].

SLIP SYSTEM RESPONSE AND DISLOCATION DENSITY EVOLUTION

The accumulation of dislocation-densities is an important microstructural characteristic that dictates material performance at high strain levels[22]. The level of immobilization generated in individual slip systems is indicative of the material's ability to deform on certain slip planes and directions. Therefore, this would be essential for understanding one of the root causes of crack nucleation. The dislocation-density data from all simulations in the database were segmented by orientation, and then further by material type (hydrided and non-hydrided). The average activation for each slip system was then developed into separate bar charts for mobile slip system activation and immobile slip system activation. Figures 17–20 show the slip systems for the parent zirconium hcp matrix, and Figs. 21–24 show the slip systems for the fcc hydrides. Tables 3 and 4 have the slip systems that correspond to each index referenced in the figures (Table 5).

Overall, the greatest slip system magnitudes of activation were observed for the 0° case. This is significant because this orientation is the preferential orientation for both dislocation mobility (sources) and immobilization. In physical terms, the 0° orientation corresponds to the material grains being oriented along the circumference of a cladding rod. This phenomenon is demonstrated at lower strain levels within hydrides (Figs. 21, 23) and is no longer as apparent at higher strain levels (Figs. 22, 24). This means that hydrides can contribute to both mobile and immobile dislocation accumulation within a material at higher strain levels, regardless of the parent material orientation. The accumulation of immobile dislocation activity within the hydrides is a driving factor for fracture at higher strain levels. Additionally, hydrides consistently had higher slip system activation than the zirconium (hcp) parent material at lower strain levels, and lower activity than the parent material at higher strain levels, for both mobile and immobile dislocation densities. However, the hcp parent material had concentrated dislocation activity across a relatively small

Table 4. HCP Slip Systems.

Basal	1	(0 0 0 1) [2 $\bar{1}$ $\bar{1}$ 0]
	2	(0 0 0 1) [$\bar{1}$ 2 $\bar{1}$ 0]
	3	(0 0 0 1) [$\bar{1}$ $\bar{1}$ 2 0]
Prismatic	4	(1 0 $\bar{1}$ 0) [$\bar{1}$ 2 $\bar{1}$ 0]
	5	(0 $\bar{1}$ 1 0) [2 $\bar{1}$ $\bar{1}$ 0]
	6	($\bar{1}$ 1 0 0) [$\bar{1}$ $\bar{1}$ 2 0]
Pyramidal <a>	7	(1 0 $\bar{1}$ 1) [$\bar{1}$ 2 $\bar{1}$ 0]
	8	(0 $\bar{1}$ 1 1) [2 $\bar{1}$ $\bar{1}$ 0]
	9	($\bar{1}$ 1 0 1) [$\bar{1}$ $\bar{1}$ 2 0]
	10	($\bar{1}$ 0 1 1) [$\bar{1}$ 2 $\bar{1}$ 0]
	11	(0 1 $\bar{1}$ 1) [2 $\bar{1}$ $\bar{1}$ 0]
	12	(1 $\bar{1}$ 0 1) [1 1 $\bar{2}$ 0]
Pyramidal <c + a>	13	(1 0 $\bar{1}$ 1) [$\bar{1}$ $\bar{1}$ 2 3]
	14	(1 0 $\bar{1}$ 1) [$\bar{2}$ 1 1 3]
	15	(0 $\bar{1}$ 1 1) [1 1 $\bar{2}$ 3]
	16	(0 $\bar{1}$ 1 1) [$\bar{1}$ 2 $\bar{1}$ 3]
	17	($\bar{1}$ 1 0 1) [2 $\bar{1}$ $\bar{1}$ 3]
	18	($\bar{1}$ 1 0 1) [1 $\bar{2}$ 1 3]
	19	($\bar{1}$ 0 1 1) [2 $\bar{1}$ $\bar{1}$ 3]
	20	($\bar{1}$ 0 1 1) [1 1 $\bar{2}$ 3]
	21	(0 1 $\bar{1}$ 1) [$\bar{1}$ $\bar{1}$ 2 3]
	22	(0 1 $\bar{1}$ 1) [1 $\bar{2}$ 1 3]
	23	(1 $\bar{1}$ 0 1) [$\bar{2}$ 1 1 3]
	24	(1 $\bar{1}$ 0 1) [$\bar{1}$ 2 $\bar{1}$ 3]

Table 5. FCC Slip Systems.

1	(1 1 1) [$\bar{1}$ 0 1]
2	(1 1 1) [$\bar{1}$ 1 0]
3	(1 1 1) [0 $\bar{1}$ 1]
4	($\bar{1}$ $\bar{1}$ 1) [0 1 1]
5	($\bar{1}$ $\bar{1}$ 1) [$\bar{1}$ 1 0]
6	($\bar{1}$ $\bar{1}$ 1) [1 0 1]
7	($\bar{1}$ 1 1) [1 0 1]
8	($\bar{1}$ 1 1) [1 1 0]
9	($\bar{1}$ 1 1) [0 $\bar{1}$ 1]
10	(1 $\bar{1}$ 1) [0 1 1]
11	(1 $\bar{1}$ 1) [1 1 0]
12	(1 $\bar{1}$ 1) [$\bar{1}$ 0 1]

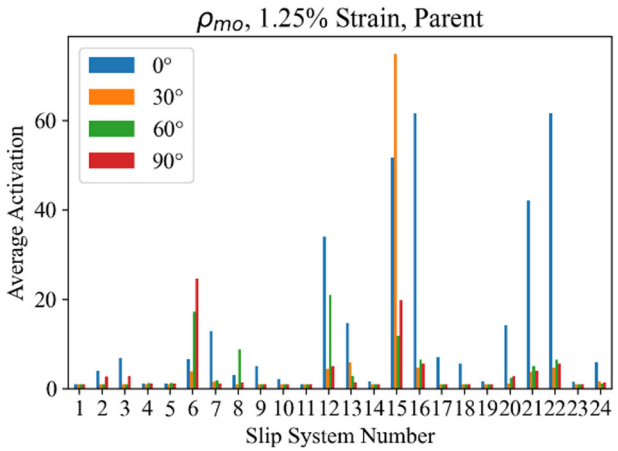

Fig. 18 Average mobile slip system activation for parent material (hcp) at 2.0% nominal strain.

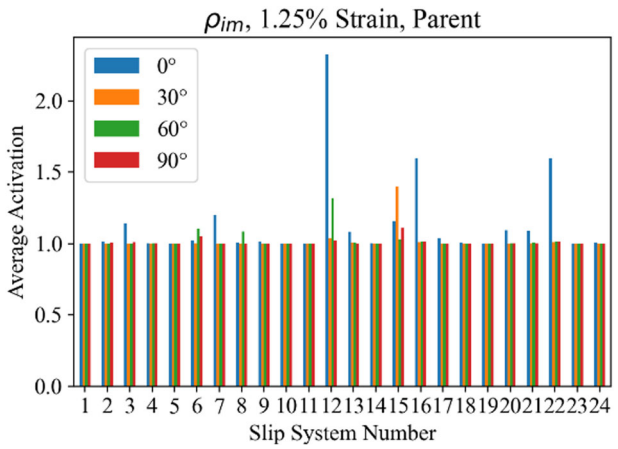

Fig. 19 Average immobile slip system activation for parent material (hcp) at 1.25% nominal strain.

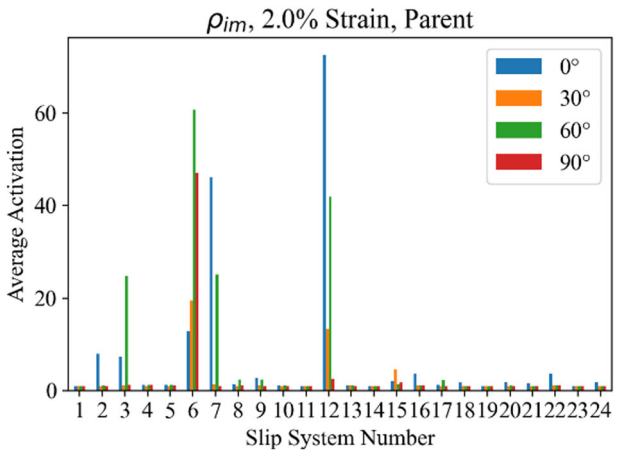

Fig. 20 Average immobile slip system activation for parent material (hcp) at 2.0% nominal strain.

number of slip systems. This indicates that the hcp parent material's ability to blunt cracks is limited to a small number of slip systems and directions that heavily depend on material orientation, whereas the fcc hydrides are more capable of serving as a dislocation source regardless of their orientation. Hence, the fcc

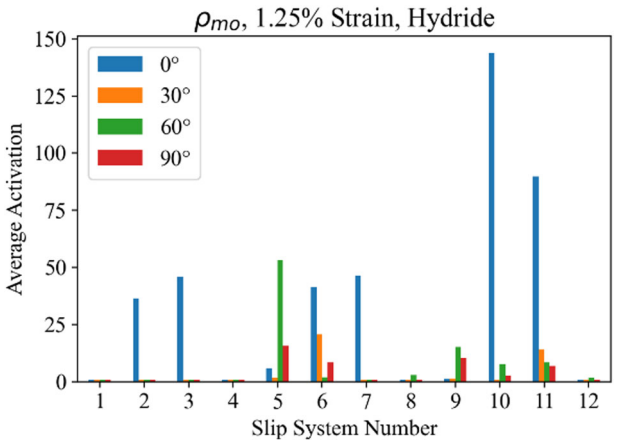

Fig. 21 Average mobile slip system activation for hydride material (fcc) at 1.25% nominal strain.

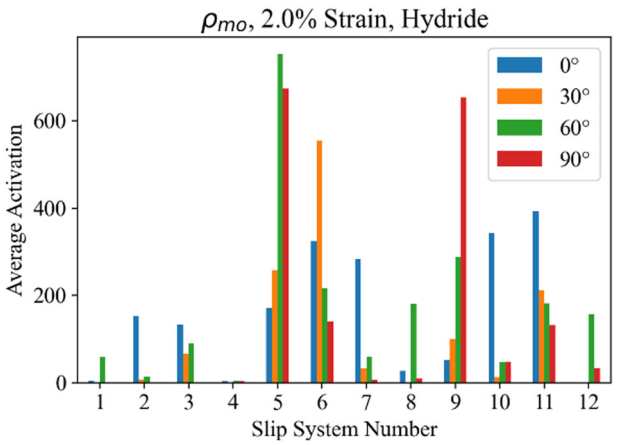

Fig. 22 Average mobile slip system activation for hydride material (fcc) at 2.0% nominal strain.

hydrides provide both (1) higher magnitudes of dislocation activation at low strains and (2) relatively similar activation regardless of parent material orientation to the loading axis.

Mobile dislocation density activity is also a significant indicator of the ductility within a material. For the parent zirconium material, the $(0\bar{1}10)$ $[2\bar{1}\bar{1}0]$, $(01\bar{1}1)$ $[2\bar{1}\bar{1}0]$, and $(0\bar{1}11)$ $[11\bar{2}3]$ slip systems displayed the greatest mobile dislocation densities throughout the strain interval from 1.25% to 2.0%. (Figs. 17,18) This indicates that a combination of prismatic and pyramidal planes is most responsible for the ductility in the parent zirconium material. For the hydrides, Figs. 21 and 22 show that most of the ductile slip activity occurs on the (1 1 1) family of planes, and that as strain levels increase, the most active systems become the $(\bar{1}\ \bar{1}$ 1) [0 1 1] and $(\bar{1}\ \bar{1}$ 1) $[\bar{1}$ 1 0] systems.

Immobilized dislocation-densities can be representative of dislocation pileups within a material that reduce ductility and eventually lead to crack nucleation. For the parent material, most active immobile slip systems correspond to the most active mobile slip systems and are a combination of prismatic and pyramidal <a> systems. The most active immobilized slip system is the pyramidal $(1\ \bar{1}\ 0\ 1)$ $[1\ 1\ \bar{2}\ 0]$ system, but this system is consistently most active for the 0° material orientation, indicating that preferential material orientations that correspond to reduced levels of dislocation pileups exist. (Figs. 17, 18) Furthermore, while the basal cleavage planes do accumulate some immobile dislocation-densities, they are not as active as the prismatic system at higher strain levels. Within the hydrides (Fig. 24), the

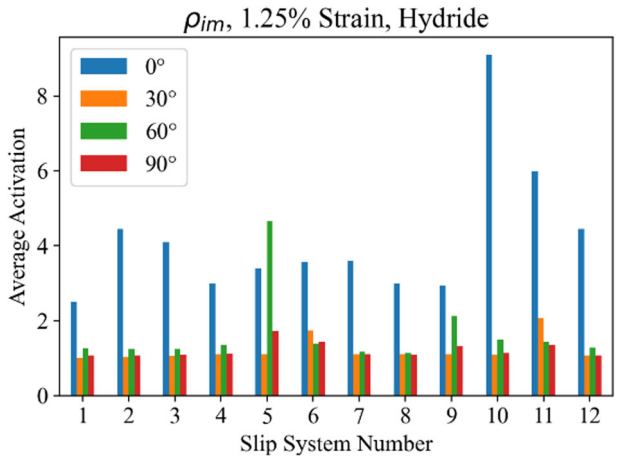

Fig. 23 Average immobile slip system activation for hydride material (fcc) at 1.25% nominal strain.

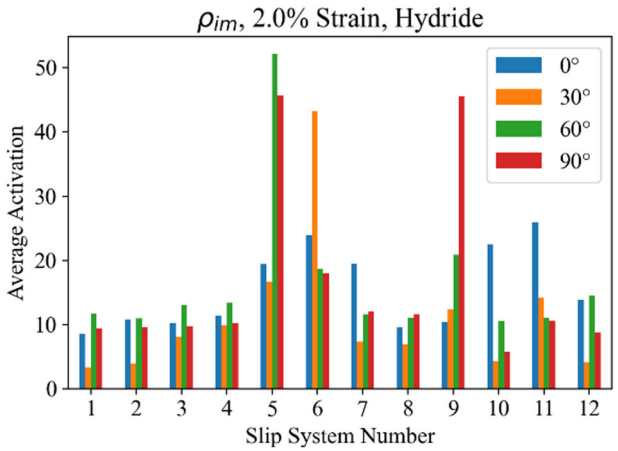

Fig. 24 Average immobile slip system activation for hydride material (fcc) at 2.0% nominal strain.

immobile slip system activation was far more uniform across all slip systems when compared with the parent material activations (Fig. 20) This is consistent with hydrides typically serving as embrittling agents where cracks form and propagate within a larger material, regardless of their orientation.

Crack nucleation predictions were obtained using a database of 210 FE deterministically obtained hydrided zirconium fracture models and a Bayesian framework. The deterministic predictions were obtained using a dislocation-density based crystalline plasticity approach and a nonlinear FE and microstructurally based fracture model. Extreme Value Theory was used to characterize the fracture nucleation critical stress and shear slip levels within the simulations, and interrelated GPRs predictions provided probabilities of fracture nucleation with uncertainty bounds for a myriad of microstructural characteristics, such as hydride orientations and distributions, texture, and crystalline structures, such that dominant mechanisms can be identified. Orientation relations between the material phases provided an accurate representation of the complex interaction between the fcc and hcp materials for these multi-crystalline and phase systems. The effects of fracture critical stress and shear slip on crack nucleation were investigated, and these were dominant characteristics related to failure.

Gumbel distributions were shown to be an accurate form for describing the extrema of the stress response of a material. The GPR ML approach was used to quantify uncertainties in the resulting ROMs. Crack nucleation was accurately predicted using both shear slip and fracture critical stress as dominant output categories. These output features are also directly related to the accumulation of immobile and mobile dislocation densities. As the GPR predictions indicate, these dislocation-densities are related to shear stain accumulation and the competing effects of crack nucleation and crack blunting. Hydride orientation is another significant factor for the likelihood of failure at lower strain levels. At specified failure strains, radial hydrides have a higher probability of failure at similar stress levels than do circumferential hydrides. Hydrides displayed the greatest dislocation-density activation at lower strain levels and serve as dislocation sources within the multiphase material. These predictions of mechanistic behavior, such as the identification of how immobile and mobile densities on specific slip systems, can only have obtained with our Bayesian based GPR predictions. Models of failure probability were used to accurately create heatmaps showing cracking likelihood.

These proposed predictions provide a needed link and coupling between validated deterministic and ML approaches for a comprehensive understanding of the crack nucleation and propagation of fracture for hydrided zirconium alloys. This approach can be used to predict failure in other multiphase materials, such as alloys with inclusions or precipitates and coated material systems, at different physical scales ranging from the nano to the micro, such that validated deterministic models can be used to generate physically accurate datasets for ML approaches, trained datasets, and ROMs.

DATA AVAILABILITY

All the relevant data for the manuscript is provided in https://github.com/tshasan-ncsu/fracture_nucleation.

Received: 4 November 2022; Accepted: 15 March 2023;
Published online: 31 March 2023

REFERENCES

1. Motta, A. T. et al. Hydrogen in Zirconium alloys: A review. *J. Nucl. Mater.* **518**, 440–460 (2019). pp.
2. Leitch, B. W. & Puls, M. P. Finite element calculations of the accommodation energy of a misfitting precipitate in an elastic-plastic matrix. *Met. Mater. Trans. A* **23**, 797–806 (1992).
3. Gong, W. et al. Hydrogen diffusion and precipitation in duplex zirconium nuclear fuel cladding quantified by high-resolution neutron imaging. *J. Nucl. Mater.* **526**, 151726–151757 (2019).
4. Birch, R., Wang, S., Tong, V. S. & Britton, T. B. The effect of cooling rate and grain size on hydride microstructure in Zircaloy-4. *J. Nucl. Mater.* **513**, 221–225 (2019).
5. Hsu, H.-H., Chiang, M.-F. & Chen, Y.-C. The Influence of hydride on fracture toughness of recrystallized Zircaloy-4 Cladding. *J. Nucl. Mater.* **447**, 1–3 (2014).
6. Pshenichnikov, A., Stuckert, J. & Walter, M. Hydride precipitation, fracture and plasticity mechanisms in pure zirconium and Zircaloy-4 at temperatures typical for the postulated loss-of-coolant accident. *Nucl. Eng. Des.* **301**, 366–377B (2016).
7. Kubo, T., Kobayashi, Y. & Uchikoshi, H. Determination of fracture strength of δ-Zirconium hydrides embedded in Zirconium Matrix at high temperatures. *J. Nucl. Mater.* **435**, 1–3 (2013).
8. Gopalan, A. et al. Effect of radial hydride on room temperature fracture toughness of Zr-2.5Nb pressure tube material. *J. Nucl. Mater.* **544**, 152681 (2021).
9. Hsu, H.-H. & Tsay, L.-W. Effect of hydride orientation on fracture toughness of Zircaloy-4 cladding. *J. Nucl. Mater.* **408**, 67–72 (2011).
10. Kim, J.-S., Kim, T.-H., Kook, D.-H. & Kim, Y.-S. Effects of hydride morphology on the embrittlement of Zircaloy-4 cladding. *J. Nucl. Mater.* **456**, 235–245 (2015).
11. Pierron, O. N., Koss, D. A., Motta, A. T. & Chan, K. S. The influence of hydride blisters on the fracture of Zircaloy-4. *J. Nucl. Mater.* **322**, 21–35 (2003).
12. Shi, S.-Q. & Puls, M. P. Fracture strength of hydride precipitates in Zr–2.5Nb alloys. *J. Nucl. Mater.* **275**, 312–317 (1999).
13. Feng, J. L., Varias, A. G. & Sui, Y. K. Finite element analysis for steady-state hydride-induced fracture in metals by composite model. *Int J. Solids Struct.* **43**, 2174–2192 (2006).
14. Shi, S. Q. & Puls, M. P. Criteria for fracture initiation at hydrides in Zirconium Alloys I. Sharp Crack Tip. *J. Nucl. Mater.* **208**, 232–242 (1994).

15. Sharma, R. K. et al. Effect of radial hydride fraction on fracture toughness of CWSR Zr-2.5%Nb pressure tube material between ambient and 300 °C temperatures. *J. Nucl. Mater.* **508**, 546–555 (2018).
16. Varias, A. G. & Massih, A. R. Hydride-induced embrittlement and fracture in metals - effect of stress and temperature distribution. *J. Mech. Phys. Solids* **50**, 1469–1510 (2002).
17. Jernkvist, L. O. Multi-field modelling of hydride forming metals Part II: Application to fracture. *Comput Mater. Sci.* **85**, 383–401 (2014).
18. Suman, S., Khan, Mohd, K., Pathak, M. & Singh, R. N. 3D simulation of hydride-assisted crack propagation in Zircaloy-4 using XFEM. *Int J. Hydrog. Energy* **42**, 18668–18673 (2017).
19. Olsson, P. A. T., Kese, K., Kroon, M. & Holston, A.-M. A. Ab initio-based fracture toughness estimates and transgranular traction-separation modelling of Zirconium hydrides. *Model Simul. Mat. Sci. Eng.* **23**, 045015–045022 (2015). 2015.
20. Salmenjoki, H., Alava, M. J. & Laurson, L. Machine learning plastic deformation of crystals. *Nat. Commun.* **9**, 5307–5316 (2018).
21. Hunter, A. et al. Reduced-order modeling through machine learning and graph-theoretic approaches for brittle fracture applications. *Comput Mater. Sci.* **157**, 87–98 (2019).
22. Mohamed, I., Hasan, T. & Zikry, M. A. Thermomechanical microstructural predictions of fracture nucleation of Zircaloy-4 alloys with δ and ε hydride distributions. *J. Eng. Mater. Technol.* **144**, 1–14 (2022).
23. Yuan, M., Paradiso, S., Meredig, B. & Niezgoda, S. R. Machine learning–based reduce order crystal plasticity modeling for ICME applications. *Integr. Mater. Manuf. Innov.* **7**, 214–230 (2018).
24. Hill, J. et al. Materials science with large-scale data and informatics: Unlocking new opportunities. *MRS Bull.* **41**, 399–409 (2016).
25. Ibragimova, O., Brahme, A., Muhammad, W., Lévesque, J. & Inal, K. A new ANN based crystal plasticity model for FCC materials and its application to non-monotonic strain paths. *Int J. Plast.* **144**, 103059–103072 (2021).
26. Naik, D. L. & Kiran, R. Identification and characterization of fracture in metals using machine learning based texture recognition algorithms. *Eng. Fract. Mech.* **219**, 106618–106626 (2019).
27. Nie, Z., Jiang, H. & Kara, L. B. Stress field prediction in cantilevered structures using convolutional neural networks. *J. Comput. Inf. Sci. Eng.* **20**, 011002–01112 (2020).
28. Wang, Z. & Zhang, Z. A Mesh-free method for interface problems using the deep learning approach. *J. Comput. Phys.* **400**, 108963–108977 (2020).
29. Zikry, M. A. A. & Kao, M. Inelastic microstructural failure mechanisms in crystalline materials with high angle grain boundaries. *J. Mech. Phys. Solids* **44**, 1765–1798 (1996).
30. Shanthraj, P. & Zikry, M. A. Dislocation density evolution and interactions in crystalline materials. *Acta Mater.* **59**, 7695–7702 (2011).
31. Mohamed, I. & Zikry, M. A. Modeling of the microstructural behavior of hydrided zirconium alloys. *Comput. Mech.* **68**, 567–578 (2021).
32. Une, K., Nogita, K., Ishimoto, S. & Ogata, K. Crystallography of Zirconium hydrides in recrystallized Zircaloy-2 fuel cladding by electron backscatter diffraction. *J. Nucl. Sci. Technol.* **41**, 731–740 (2004).
33. Wu, Q. & Zikry, M. A. Microstructural modeling of crack nucleation and propagation in high strength martensitic steels. *Int J. Solids Struct.* **51**, 4345–4356 (2014).
34. Virtanen, P. et al. SciPy 1.0: Fundamental algorithms for scientific computing in Python. *Nat. Methods* **17**, 261–272 (2020).
35. Pedregosa, F. et al. Scikit-Learn: Machine learning in Python. *J. Mach. Learn. Res.* **12**, 852825–852830 (2011).
36. Morris, M. D. Factorial sampling plans for preliminary computational experiments. *Technometrics* **33**, 161–174 (1991).
37. Herman, J. & Usher, W. SALib: An open-source Python library for sensitivity analysis. *J. Open Source Softw.* **2**, 97–105 (2017).
38. Hatem, T. M. & Zikry, M. A. Modeling of Lath martensitic microstructures and failure evolution in steel alloys. *J. Eng. Mater. Technol.* **131**, 041207-1–041207-10 (2009).
39. Vicente Alvarez, M. A., Santisteban, J. R., Vizcaíno, P., Ribárik, G. & Ungar, T. Quantification of dislocations densities in Zirconium hydride by X-ray line profile analysis. *Acta Mater.* **117**, 1–12 (2016).
40. Elkhodary, K. I. & Zikry, M. A. Dynamic crack nucleation, propagation, and interactions with crystalline secondary phases in aluminum alloys subjected to large deformations. *Philos. Mag.* **92**, 3920–3949 (2012).

ACKNOWLEDGEMENTS

Support from the DOE NEUP Integrated Research Project IRP-17-13708, Development of a Mechanistic Hydride Behavior Model for Spent Fuel Cladding Storage and Transportation, is gratefully acknowledged by all three authors.

AUTHOR CONTRIBUTIONS

All three authors contributed equally to this manuscript.

COMPETING INTERESTS

The authors declare no competing interests.

ADDITIONAL INFORMATION

Correspondence and requests for materials should be addressed to Tamir Hasan, Laurent Capolungo or Mohammed Zikry.

Reprints and permission information is available at http://www.nature.com/reprints

Publisher's note Springer Nature remains neutral with regard to jurisdictional claims in published maps and institutional affiliations.